

# 4D deformable models with temporal constraints: application to 4D cardiac image segmentation

Johan Montagnat<sup>a,b,\*</sup>, Hervé Delingette<sup>a</sup>

<sup>a</sup> EPIDAURE, INRIA, 2004 route des lucioles, BP 93, 06902 Sophia Antipolis cedex, France

<sup>b</sup> CREATIS, CNRS UMR 5515, Inserm 20 av. A. Einstein, 69621 Villeurbanne cedex, France

Received 20 February 2001; received in revised form 29 July 2003; accepted 20 June 2004

Available online 5 November 2004

## Abstract

Segmentation of time series of 3D cardiac images is clinically used for the assessment of the mechanical function of the left ventricle. To take into account the 4D (3D + T) nature of those images, we propose to extend the deformable surface framework by introducing time-dependent constraints. Thus, in addition to computing an internal force for enforcing the regularity of the deformable model, prior motion knowledge is introduced in the deformation process through either temporal smoothing or trajectory constraints.

In this paper, deformable surfaces are represented as simplex meshes owing to their generality and their ability to compute mean curvature at each vertex. The segmentation accuracy of this 4D deformable model is estimated on synthetic SPECT image sequences for which a ground truth about the LV volume is known. Segmentation of non-synthetic SPECT and other modalities 4D images is also discussed.

© 2004 Elsevier B.V. All rights reserved.

**Keywords:** Segmentation; Shape; Temporal constraint; 4D image; Heart; SPECT

## 1. Context

Medical image segmentation is a prerequisite for many high-level tasks such as images analysis, computer-assisted diagnosis, geometric modeling of anatomical structures, or the construction of bio-mechanical models used for surgery simulation. However, image segmentation remains one of the open issues in medical image analysis. Indeed, poor image quality, low contrast, presence of decoy structures and the complex nature of the shape and appearance of some anatomical structures may lead to a poor accuracy or robustness of image segmentation algorithms.

Among the large collection of existing segmentation algorithms, approaches based on deformable surface have been extensively studied (Frangi et al., 2001; Montagnat et al., 2001) for the delineation of tridimensional structures. The main incentive in using deformable models is the introduction of a priori knowledge about the shape and appearance of the target structures. Thus, they are mainly suited for segmenting structures having a “typical” shape (i.e., for which one can perform statistical shape analysis) and that appear with a low to medium contrast in images (since more direct bottom-up techniques can apply otherwise). Furthermore, they offer an attractive solution for performing automated or semi-automated segmentation of large databases of images.

In this paper, we propose an extension of deformable surfaces based segmentation to the case of time series of 3D medical images (in the remainder qualified as 4D

\* Corresponding author. Present address: ESSI RAINBOW, 930 route des Colles, BP 145 06903 Sophia Antipolis Cedex, France. Tel.: +33 492 96 51 03; fax: +33 492 96 50 55.

E-mail address: [johan@creatis.insa-lyon.fr](mailto:johan@creatis.insa-lyon.fr) (J. Montagnat).

images). We demonstrate the relevance of this approach with a case study on the segmentation of cardiac images although our technique is generic enough to be applicable to other 4D image segmentation problems.

## 2. Previous work

### 2.1. Segmentation and tracking of cardiac images

The segmentation and tracking of the left ventricle (LV) in 2D, 3D or 4D images have been the motivation of many research works. We only consider in this section those related to the segmentation of 4D images.

A recent survey (Frangi et al., 2001) shows the relevance of deformable models approaches for LV segmentation due to their ability to introduce prior knowledge. Authors have based their models on different geometric and physical representations, including spring-mass models (Nastar and Ayache, 1996), triangle-based finite element models (Park et al., 1996; McInerney and Terzopoulos, 1995), simplex meshes (Montagnat et al., 1999; Gérard et al., 2002), tetrahedral finite element models (Pham et al., 2001; Sermesant et al., 2002; Papademetris et al., 2001), level sets (Charnoz et al., 2003; Paragios, 2002; Lin et al., 2002), 3D B-Spline deformation fields (Bardinet et al., 1996; Chandrashekar et al., 2003) and statistical shape and appearance models (Frangi et al., 2002; Üzümcü et al., 2003).

When dealing with the processing of 4D cardiac images, one has to solve two simultaneous problems: a segmentation problem consisting in the delineation of the LV in each image and a tracking problem consisting in recovering the adequate trajectories of material points. Both problems are naturally coupled which implies that the LV segmentation should take into account the fact that the LV is a moving structure and not a static one.

The temporal dimension of cardiac imaging has been neglected in many research work (Bardinet et al., 1996; McInerney and Terzopoulos, 1995; Montagnat et al., 1999) by resorting to a sequential segmentation of images, the output of the previous instant serving as the initial guess for the current instant. Those algorithms are straightforward extensions of volumetric image segmentation algorithms and require no additional resource in terms of memory and computation. However, they generally lead to an underestimation of the cardiac motion.

A weak level of temporal coherence can be introduced by adding in the external energy a term enforcing the temporal consistency of image intensity (Paragios, 2002) or isophote curvature (Benayoun and Ayache, 1998). More a priori knowledge about the LV motion can be included by using principal component analysis (Chandrashekar et al., 2003; Üzümcü et al., 2003), or

motion models built from the statistical analysis of tagged MR imaging (Gérard et al., 2002) or from a patient-based electromechanical model (Sermesant et al., 2002). Declerck et al. (1998), define a 4D planispheric transformation taking into account the continuity, and possibly the periodicity, of the time dimension.

In this paper, we propose a generic and versatile extension of the deformable model framework for the segmentation and tracking of 4D images. This extension consists in the introduction of a temporal constraint where a priori knowledge about the motion of the structure of interest can be specified in a weak or strong manner.

### 2.2. Robustness issues

A common drawback of deformable models is their lack of robustness linked with the local minima problem: the algorithm converges towards undesired shapes that do not correspond to the global minimum of a functional. In a nutshell, the number of local minima of a functional defined on a deformable model is directly related to the number of *Degrees Of Freedom* (DOF) of that model. To represent an object with enough details, one may want to use a mesh representation with a high number of vertices leading to a functional with many local minima. This may cause the mesh evolution to very sensitive to the presence of noise and outliers. In such cases, it is necessary to control the extent of the mesh deformation by eventually restricting its number of DOF. Note that the model evolution is not only important for robustness issues but also for enforcing the homology at important anatomical points between the template surface and the segmented one.

Several methods have been proposed in the literature to control the extent of deformation in a deformable model. Surface deformation methods can be classified into parameterized deformations (Terzopoulos and Metaxas, 1991; Vemuri and Radisavljevic, 1993) and global deformations (Besl and McKay, 1992; Bardinet et al., 1996; Lötjönen et al., 1999). To improve this point, we have introduced a coarse-to-fine deformation scheme in (Montagnat and Delingette, 1998) that does not rely on complex and computationally expensive stochastic global minimization techniques: we start with the coarse description with few DOF in order to achieve robustness while a fine description using a large number of DOF is used to achieve an accurate reconstruction. The extension of this approach to 4D deformable models is described in Section 4.

## 3. Model description

Among the possible geometric representations of deformable surfaces (see (McInerney and Terzopoulos,

1996 or Montagnat et al., 2001) for a review of surface geometric representations), we rely on a discrete surface model called *simplex mesh* introduced by Delingette (1999). Its main advantage is to achieve a stable computation of curvature-based internal forces.

Furthermore, its simple data structure leads to an efficient computation of deformation and a limited memory storage. This last point is specifically important in the case of 4D deformable models, where  $n$  surface meshes must be updated at each iteration.

### 3.1. Simplex mesh geometry

We briefly recall the main geometric notions defined on simplex meshes. These notions are used in the definitions of regularizing forces. A surface simplex mesh is composed of a set of  $d$  vertices  $\{\mathbf{p}_i\}_{i \in [0, d-1]}$ , each vertex being connected to exactly three neighbors. Simplex meshes are topologically dual to triangulations as illustrated on the left side of Fig. 1 showing a simplex mesh (solid line) and its dual triangulation (dashed line). Geometric quantities can be derived from basic geometric reasoning. The right side of Fig. 1 diagrams a vertex  $\mathbf{p}_i$  of a simplex mesh and its three neighbors,  $\mathbf{p}_{\text{ngh}_j(i)}$ ,  $j \in \{1, 2, 3\}$ . Let  $\mathcal{P}_i$  be the plane defined by  $\mathbf{p}_i$ 's three neighbors. We denote  $\mathbf{p}_i^\perp$  the projection of  $\mathbf{p}_i$  on  $\mathcal{P}_i$  and  $\mathbf{n}_i$  the unit normal vector of  $\mathcal{P}_i$ . We introduce the circumscribed circle to triangle  $(\mathbf{p}_{\text{ngh}_1(i)}, \mathbf{p}_{\text{ngh}_2(i)}, \mathbf{p}_{\text{ngh}_3(i)})$  with center  $\mathbf{c}_i$  and radius  $r_i$ , and the circumscribed sphere to vertices  $(\mathbf{p}_i, \mathbf{p}_{\text{ngh}_1(i)}, \mathbf{p}_{\text{ngh}_2(i)}, \mathbf{p}_{\text{ngh}_3(i)})$  with center  $\mathbf{o}_i$  and radius  $R_i$ .

We call *metric parameters* the mass coordinates  $\varepsilon_i^1$ ,  $\varepsilon_i^2$ , and  $\varepsilon_i^3 = 1 - \varepsilon_i^1 - \varepsilon_i^2$  of  $\mathbf{p}_i^\perp$  with respect to  $\mathbf{p}_i$ 's neighbors. They control the relative position of  $\mathbf{p}_i^\perp$  in  $\mathcal{P}_i$ :

$$\mathbf{p}_i^\perp = \sum_{j=1}^3 \varepsilon_i^j \mathbf{p}_{\text{ngh}_j(i)}.$$

The *simplex angle*  $\varphi_i \in [-\pi, \pi]$  is defined by

$$\begin{cases} \sin(\varphi_i) = \frac{r_i}{R_i} \text{sign}((\mathbf{p}_{\text{ngh}_1(i)} - \mathbf{p}_i) \cdot \mathbf{n}_i), \\ \cos(\varphi_i) = \frac{\|\mathbf{c}_i - \mathbf{o}_i\|}{R_i} \text{sign}((\mathbf{c}_i - \mathbf{o}_i) \cdot \mathbf{n}_i). \end{cases}$$

It controls the elevation of vertex  $\mathbf{p}_i$  above  $\mathcal{P}_i$ . We define a vertex discrete mean curvature as  $H_i = \frac{\sin(\varphi_i)}{r_i}$ ,  $|H_i| = \frac{1}{R_i}$ . Under some assumptions, it can be shown (Delingette, 1994) that the discrete mean curvature at a vertex of a mesh lying on a continuous and sufficiently differentiable surface, converges towards the surface mean curvature at that vertex position.

The vertex position  $\mathbf{p}_i$  is uniquely defined by its three neighbors, its metric parameters and its simplex angle:

$$\mathbf{p}_i = \left( \sum_{j=1}^3 \varepsilon_i^j \mathbf{p}_{\text{ngh}_j(i)} \right) + h(\mathbf{p}_{\text{ngh}_j(i)}, \varepsilon_i^j, \varphi_i) \mathbf{n}_i.$$

where

$$h = \frac{(r_i^2 - d_i^2) \tan(\varphi_i)}{\varepsilon \sqrt{r_i^2 + (r_i^2 - d_i^2) \tan(\varphi_i)^2} + r_i},$$

$$\varepsilon = \begin{cases} 1 & \text{if } |\varphi_i| < \frac{\pi}{2} \\ -1 & \text{if } |\varphi_i| > \frac{\pi}{2} \end{cases}, \quad d_i = \|\mathbf{p}_i^\perp - \mathbf{c}_i\|. \quad (1)$$

It has been shown, in (Delingette, 1994), that a simplex mesh shape is defined up to a similarity transformation by the set of its metric parameters and simplex angles  $\{\varepsilon_i^1, \varepsilon_i^2, \varphi_i\}_i$ .

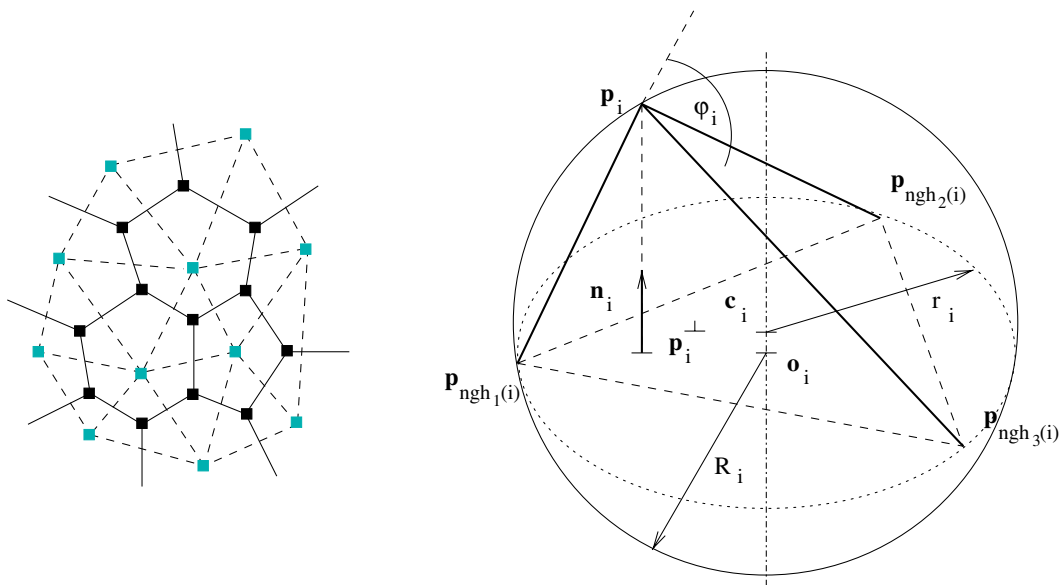


Fig. 1. Left: duality between simplex meshes and triangulations. Right: geometric definitions on a simplex mesh.

### 3.2. 4D deformable models

Since a 4D image  $I$  is a discrete set of  $n$  volumetric images defined at  $n$  different instants  $\{I_t\}_{t \in [0, n-1]}$ , we propose to define a 4D deformable surface as a set of  $n$  3D deformable surfaces  $\{\mathcal{S}_t\}_{t \in [0, n-1]}$ . As illustrated in Fig. 2, all  $n$  surface meshes  $\mathcal{S}_t$  have the same topology, i.e., there is a one to one correspondence between each vertex of the  $n$  meshes. We can therefore use the notation  $\mathbf{p}_{i,t}$  to denote the position of vertex number  $i$  at time  $t$ . We make a clear distinction between the time variable  $t$  associated with the time label in the 4D image and the time variable  $\tau$  corresponding to the synchronized evolution of all deformable surfaces from their initial shape to their final shape. The  $t$ -evolution of a mesh corresponds to motion observed in the time series of images (for instance from diastole to systole for cardiac imaging) while the  $\tau$  evolution corresponds to the minimization of a global functional. Thus, each surface  $\mathcal{S}_t$  evolves in space but remains at its temporal position  $t$  (i.e., each vertex position  $\mathbf{p}_{i,t}$  is changed in 3D space but  $t$  never changes). We make the further hypothesis that the topology of all meshes never changes during its  $\tau$ -evolution which is not in practice an important restriction.

The ordered set of vertices  $\{\mathbf{p}_{i,t}\}_{t \in [0, n-1]}$  represents the *trajectory* of the vertex  $i$  along time. It is important to note that the trajectory  $\{\mathbf{p}_{i,t}\}_t$  of a vertex may not correspond to the trajectory of physical points of the recovered anatomical structures. Trajectories are used as a mathematical support to compute temporal constraints but they only provide an apparent motion which may

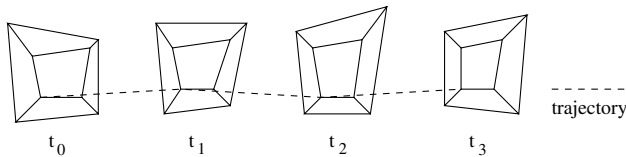


Fig. 2. Example of a 4D simplex mesh: there is a one-to-one correspondence between vertices over time  $t$ .

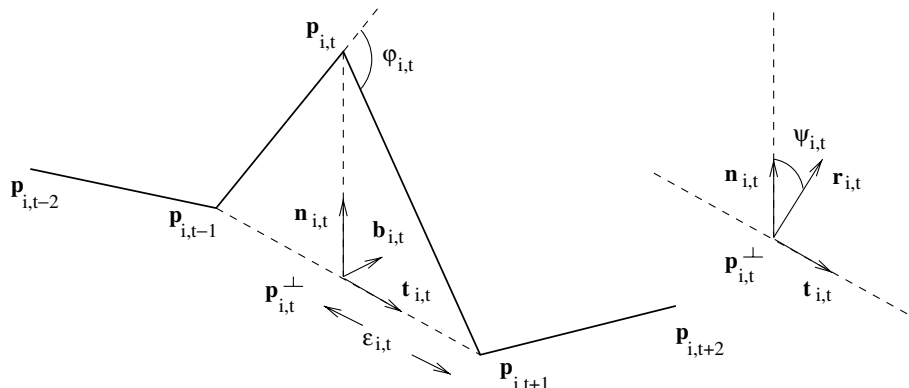


Fig. 3. Trajectory geometry.

not be the true motion of material points (this is the classical aperture problem).

Fig. 3 illustrates the computation of geometric quantities characterizing the trajectory of each vertex. From a geometrical point of view, trajectory  $\{\mathbf{p}_{i,t}\}_t$  represents a discrete line in  $\mathbb{R}^3$ . Each vertex  $\mathbf{p}_{i,t}$  has two temporal neighbors associated with the previous and following instants,  $\mathbf{p}_{i,t-1}$  and  $\mathbf{p}_{i,t+1}$ . We consider that trajectories are closed, i.e.,  $p_{i,n-1} = p_{i,0}$  and  $p_{i,n} = p_{i,0}$  when the motion is known to be periodic (which is the case for cardiac motion).

Let  $\mathbf{p}_{i,t}^\perp$  denote the orthogonal projection of  $\mathbf{p}_{i,t}$  onto segment  $[\mathbf{p}_{i,t-1}, \mathbf{p}_{i,t+1}]$ . The position of point  $\mathbf{p}_{i,t}$  relatively to its temporal neighbors may be defined through three geometric parameters:

- a metric parameter  $\varepsilon_{i,t} \in [0, 1]$  measuring the relative position of  $\mathbf{p}_{i,t}^\perp$  in  $[\mathbf{p}_{i,t-1}, \mathbf{p}_{i,t+1}]$  ( $\mathbf{p}_{i,t}^\perp = \varepsilon_{i,t}\mathbf{p}_{i,t-1} + (1 - \varepsilon_{i,t})\mathbf{p}_{i,t+1}$ );
- an angle  $\varphi_{i,t}$  measuring the elevation of  $\mathbf{p}_{i,t}$  above the segment  $[\mathbf{p}_{i,t-1}, \mathbf{p}_{i,t+1}]$  in plane  $(\mathbf{p}_{i,t-1}, \mathbf{p}_{i,t}, \mathbf{p}_{i,t+1})$ ;
- an angle  $\psi_{i,t}$  measuring the discrete torsion of the trajectory.

Intuitively,  $\varepsilon_{i,t}$ ,  $\varphi_{i,t}$ , and  $\psi_{i,t}$  correspond to discrete arc length, curvature, and torsion respectively. Let  $\mathbf{t}_{i,t}$  denote the discrete tangent,  $\mathbf{b}_{i,t}$  the binormal vector, and  $\mathbf{n}_{i,t}$  the discrete normal to point  $\mathbf{p}_{i,t}$ , respectively:

$$\mathbf{t}_{i,t} = \frac{\mathbf{p}_{i,t-1}\mathbf{p}_{i,t+1}}{\|\mathbf{p}_{i,t-1}\mathbf{p}_{i,t+1}\|}, \quad \mathbf{b}_{i,t} = \frac{\mathbf{p}_{i,t}\mathbf{p}_{i,t+1} \wedge \mathbf{p}_{i,t-1}\mathbf{p}_{i,t}}{\|\mathbf{p}_{i,t}\mathbf{p}_{i,t+1} \wedge \mathbf{p}_{i,t-1}\mathbf{p}_{i,t}\|},$$

$$\mathbf{n}_{i,t} = \mathbf{b}_{i,t} \wedge \mathbf{t}_{i,t}.$$

The metric parameter, the elevation angle, and the torsion angle are defined by

$$\varepsilon_{i,t} = \frac{\|\mathbf{p}_{i,t}^\perp\mathbf{p}_{i,t+1}\|}{\|\mathbf{p}_{i,t-1}\mathbf{p}_{i,t+1}\|},$$

$$\varphi_{i,t} = (\mathbf{p}_{i,t}\mathbf{p}_{i,t+1}, \widehat{\mathbf{p}_{i,t-1}\mathbf{p}_{i,t}}),$$

$$\psi_{i,t} \text{ such that } \mathbf{n}_i = \cos(\psi_{i,t})\mathbf{r}_{i,t} + \sin(\psi_{i,t})\mathbf{t}_{i,t} \wedge \mathbf{r}_{i,t}$$

with

$$\mathbf{r}_{i,t} = \frac{\mathbf{t}_{i,t} \wedge (\mathbf{p}_{i,t-2} \mathbf{p}_{i,t-1} \wedge \mathbf{p}_{i,t+1} \mathbf{p}_{i,t+2})}{\|\mathbf{t}_{i,t} \wedge (\mathbf{p}_{i,t-2} \mathbf{p}_{i,t-1} \wedge \mathbf{p}_{i,t+1} \mathbf{p}_{i,t+2})\|}.$$

### 3.3. Law of motion

A deformable surface deforms under the combined action of a regularization (or internal) term and a data (or external) term enforcing the attraction of the surface towards the apparent structure boundary in the image. The regularization force is usually a geometric regularity constraint imposing some level of smoothness. To take into account, the time continuity in the image sequence, an additional force, the *temporal force* is considered to enforce the temporal coherence of the deformations across the time sequence  $t$ . This temporal force is computed independently and with a different formulation since the time dimension  $t$  is very different from the spatial dimensions. Indeed, the time dimension might be periodic (as for the cardiac cycle), is discrete, and the sampling frequency in time is usually very small compared to the spatial sampling.

The law of motion governing the evolution of all  $d \times n$  vertices is based on a classical Newtonian (or second-order evolution) framework resulting, in the following set of equations:

$$\begin{aligned} m(i) \frac{d^2 \mathbf{p}_{i,t}}{d\tau^2} + \gamma \frac{d\mathbf{p}_{i,t}}{d\tau} - \alpha(i) f_{\text{int}}(\mathbf{p}_{i,t}) - \delta(i) f_{\text{time}}(\mathbf{p}_{i,t}) \\ = \beta(i) f_{\text{ext}}(\mathbf{p}_{i,t}), \end{aligned} \quad (2)$$

where  $m(i)$  is the  $i$ th vertex mass;  $\gamma$  is the background damping parameter;  $f_{\text{int}}(\mathbf{p}_{i,t})$  is the spatial regularizing force;  $f_{\text{time}}(\mathbf{p}_{i,t})$  is the temporal regularizing force;  $f_{\text{ext}}(\mathbf{p}_{i,t})$  is the data force;  $\alpha(i)$ ,  $\delta(i)$ , and  $\beta(i)$  are weights controlling the spatial, temporal, and external terms.

Again, in this equation,  $\tau$  designates a temporal variable controlling the evolution of a model from its initial shape toward its final shape. The discretization of Eq. (2) using an fully explicit discretization scheme leads to

$$\begin{aligned} \mathbf{p}_{i,t}^{\tau+\Delta\tau} = \mathbf{p}_{i,t}^{\tau} + (1 - \gamma)(\mathbf{p}_{i,t}^{\tau} - \mathbf{p}_{i,t}^{\tau-\Delta\tau}) + \alpha_i f_{\text{int}}(\mathbf{p}_{i,t}^{\tau}) \\ + \delta_i f_{\text{time}}(\mathbf{p}_{i,t}^{\tau}) + \beta_i f_{\text{ext}}(\mathbf{p}_{i,t}^{\tau}), \end{aligned} \quad (3)$$

where  $\alpha_i$ ,  $\delta_i$  and  $\beta_i$  are force weights including the vertex mass and the time step. The stability of this scheme is guaranteed if  $\alpha_i$ ,  $\delta_i$ ,  $\beta_i$  and  $\gamma$  range inside  $[0, \frac{1}{2}]$ ,  $[0, \frac{1}{2}]$ ,  $[0, 1]$  and  $[0, 1]$ , respectively. In all our experiments,  $\gamma$  is set to a constant value  $\gamma = 0.35$  based on an empirical study showing that it optimizes the convergence speed in general. The  $\alpha$  value is always set to 1 while the  $\delta$  value is set to 0.1. The  $\beta$  parameter weights the influence of the external versus internal and temporal forces. The  $\alpha$ ,  $\beta$  and  $\delta$  parameters have the same values for all vertices.

## 4. Globally constrained deformations of the 4D model

In order to improve the robustness of the segmentation, we rely on a coarse-to-fine approach that combines the deformable model scheme described above and the ICP algorithm (Besl and McKay, 1992) extensively used in registration frameworks. In (Montagnat and Delingette, 1998), we have shown that this approach can smoothly control the number of degrees of freedom (DOF) of deformable surfaces in an efficient and simple manner. We extend below the concept of *globally constrained deformations* to the case of 4D deformable models.

The ICP algorithms iteratively estimates a global transformation  $T$  and then applies that transformation  $T$  on the current position of the mesh. The transformation  $T$  is determined by the minimization of a least-square criterion that can be interpreted as the distance between the expected mesh position and current estimate of image boundary points. With the notations introduced above, and based on (Montagnat and Delingette, 1998) the optimal transformation  $T$  is computed as

$$T = \arg \min_{T \in T_{\text{reg}}} \left\{ \sum_{t=0}^{n-1} \sum_{i=0}^{d-1} \|T(\mathbf{p}_{i,t}) - (\mathbf{p}_{i,t} + f_{\text{ext}}(\mathbf{p}_{i,t}))\|^2 \right\}, \quad (4)$$

where  $\{\mathbf{p}_{i,t} + f_{\text{ext}}(\mathbf{p}_{i,t})\}_{\{i,t\}}$  is the current estimate of boundary points and  $T_{\text{reg}}$  is a given group of transformations with a small number of DOF. Most widely used transformation groups are the groups of rigid transformations (6 DOF), similarities (7 DOF) and affine transformations (12 DOF). For these three transformation groups, there exists a closed form solution for solving equation (4) (see (Pennec, 1996) for details). Note that to take into account of the whole time sequence, the global transformation is estimated using all instants simultaneously. However,  $T$  is a transformation of  $\mathbb{R}^3$  to avoid a distortion of the model in the time dimension.

The iterative estimation and application of transformation  $T$  leads to the ICP-based global registration of the initial template. To slowly increase the number of DOF we propose to combine the ICP approach with the local deformation scheme of equation (3), involving all DOF. For this purpose, we introduce a *global force* applied on vertex  $\mathbf{p}_i$  at time  $t$  defined as displacement produced by the global registration:

$$f_{\text{global}}(\mathbf{p}_{i,t}) = T(\mathbf{p}_{i,t}) - \mathbf{p}_{i,t}.$$

By weighting this force with a *locality* parameter  $\lambda \in [0, 1]$ , we can propose a new evolution law suitable for a coarse-to-fine deformation:

$$\begin{aligned} \mathbf{p}_{i,t}^{\tau+\Delta\tau} &= \mathbf{p}_{i,t}^{\tau} + (1 - \gamma)(\mathbf{p}_{i,t}^{\tau} - \mathbf{p}_{i,t}^{\tau-\Delta\tau}) \\ &+ (1 - \lambda)f_{\text{global}}(\mathbf{p}_{i,t}^{\tau}) + \lambda(\alpha_i f_{\text{int}}(\mathbf{p}_{i,t}^{\tau}) \\ &+ \delta_i f_{\text{time}}(\mathbf{p}_{i,t}^{\tau}) + \beta_i f_{\text{ext}}(\mathbf{p}_{i,t}^{\tau})). \end{aligned} \quad (5)$$

When  $\lambda = 0$ , the deformation is only global and the model deforms according to the ICP framework (with an additional inertia effect). Conversely, if  $\lambda = 1$ , the model deforms with its full number of DOF, i.e., with a small correlation between vertex motion. Any intermediate value of  $\lambda$  produces local deformations with a global constraint, or *globally constrained deformations*.

The complete deformation process is based on a continuous evolution from global, to highly constrained, to local deformations. This coarse-to-fine evolution improves the model convergence similarly to the *Graduated Non-Convexity* algorithm of Blake and Zisserman (1987).

## 5. Spatial and temporal shape constraints

In this section, we detail the computation of internal and temporal forces. Depending on the availability of a prior shape, internal forces can impose a weak or strong prior knowledge, as summarized in Table 1. When no specific information is known about the shape of the structure of interest, one usually uses basic geometric assumptions such as curvature continuity to constraint the deformable model shape. When the average shape is available, then one can use this information to constrain the shape model to be close to that reference shape.

We propose to extend this distinction between weak and strong prior to the case of temporal forces. More precisely if there is no information about the expected motion of the structure, then it is possible to constrain the vertex motion such as to minimize the kinetic energy of the system (which is equivalent to perform temporal position averaging). On the contrary if the expected motion is known then vertex trajectories can be constrained to stay close to their reference shape.

### 5.1. Internal forces computation

Due to its discrete nature, the regularization of a simplex mesh is not based on the evaluation of surface partial derivatives but on the relative position of a vertex

with respect to its neighbors, i.e., in terms of metric parameters and simplex angles. More precisely, each vertex  $\mathbf{p}_i$  is attracted toward a position  $\tilde{\mathbf{p}}_i$  that locally maximizes a smoothness criterion. Let  $\tilde{\varepsilon}_i^j$ ,  $\tilde{\varphi}_i$  and  $\tilde{\mathbf{p}}_i^\perp$  denote the metric parameters, the simplex angle and the projection of  $\tilde{\mathbf{p}}_i$  on  $\mathcal{P}_i$ , respectively. The internal force can be decomposed as the sum of a tangential and a normal component:

$$\begin{aligned} f_{\text{int}}(\mathbf{p}_i) &= (\tilde{\mathbf{p}}_i^\perp - \mathbf{p}_i^\perp) + (h(\mathbf{p}_{\text{ngh}_j(i)}, \tilde{\varepsilon}_i^j, \varphi_i) \\ &- h(\mathbf{p}_{\text{ngh}_j(i)}, \tilde{\varepsilon}_i^j, \tilde{\varphi}_i))\mathbf{n}_i, \end{aligned}$$

where  $h$  is defined in Eq. (1).

The tangential component of the internal force controls the vertex spacing over the surface. To ensure uniformly spread vertices, metric parameters are set to  $1/3$ :  $\tilde{\varepsilon}_i^1 = \tilde{\varepsilon}_i^2 = \tilde{\varepsilon}_i^3 = \frac{1}{3}$ . The normal component constrains the mean curvature of the surface through the simplex angle. The definition of  $\tilde{\varphi}_i$  depends on the level of geometric regularity to be enforced.

Let  $\mathcal{N}_s(i)$  be the set of all vertices connected to the vertex of index  $i$  by a path of topological length less than  $s$  edges. The scale parameter,  $s$ , defines the neighborhood size over which the mesh is regularized. For medical image segmentation we usually consider either a (weak) smoothing constraint enforcing the  $C^2$  continuity of the surface or a (strong) shape constraint:

- *Smoothing (weak spatial) constraint.*

To ensure that the vertex discrete mean curvature converges toward the weighted average mean curvature of its neighborhood, we set

$$\tilde{\varphi}_i = \arcsin \left( r_i \sum_{j \in \mathcal{N}_s(i)} e_{ij} \frac{\sin(\varphi_j)}{r_j} \right), \quad \text{with} \quad \sum_{j \in \mathcal{N}_s(i)} e_{ij} = 1.$$

This smoothness constraint is used when no anatomical shape information is available. A mesh only submitted to this constraint would converge toward a shape of constant curvature: a sphere. Note that this constraint does not entail any shrinking effect unlike the classical snake smoothing forces (Delingette, 1999).

- *Shape (strong spatial) constraint.*

Let  $\{\varphi_i^\circ\}_i$  be the set of simplex angles defining the reference shape of an anatomical structure. By setting  $\tilde{\varphi}_i = \varphi_i^\circ$ , one constrains the shape of the deformable surface to stay close to the reference shape. Furthermore, this formulation can be extended to include a scale parameter  $s$  to control the spatial extension of that constraint.

### 5.2. Temporal forces computation

Temporal forces impose some level of spatial regularity of the motion of each vertex. In other words, those

Table 1  
Spatial and temporal constraints depending on available priors

	Spatial constraint	Temporal constraint
Weak prior	Curvature-based shape smoothing	Temporal position averaging
Strong prior	Shape constraint	Trajectory constraint

forces constrain the geometric smoothness of vertex trajectories. The formulation of temporal forces closely follows that of internal forces. More precisely, under the action of this temporal force, a vertex  $\mathbf{p}_{i,t}$  is attracted toward a point  $\tilde{\mathbf{p}}_{i,t}$  lying on an optimal trajectory:  $f_{\text{time}}(\mathbf{p}_{i,t}) = \tilde{\mathbf{p}}_{i,t} - \mathbf{p}_{i,t}$ . Once again, we propose two formulations of temporal forces:

- *Smoothing (weak temporal) constraint.*

A vertex at time  $t$  is attracted toward the centroid of its two temporal neighbors:  $\tilde{\mathbf{p}}_{i,t} = \frac{\mathbf{p}_{i,t-1} + \mathbf{p}_{i,t+1}}{2}$ . Applying this force is equivalent to minimizing the kinetic energy of the 4D model. Under the unique action of this force, all vertex trajectories converge toward a straight line (a single point if the motion is periodic).

- *Trajectory (strong temporal) constraint.*

When prior knowledge about the mesh motion is known, we propose temporal forces that constrain the shape of each vertex trajectory to closely resemble that of its reference trajectory. To store those reference trajectories, one could store the  $n$  vertex positions  $\{\mathbf{p}_{i,t}\}_{t \in [0,n-1]}$  over time. However, this representation would imply that the trajectory orientation and scale is constant between images, which may not be the case. Instead, we choose to store the shape of the trajectory (invariant up to a similarity transformation) as the set of geometric parameters  $\{\tilde{\epsilon}_{i,t}, \tilde{\varphi}_{i,t}, \tilde{\psi}_{i,t}\}_{(i,t)}$  corresponding to the discrete arc-length, curvature and torsion, as described in Section 3.2. The definition of the temporal force is completed when specifying the computation of the target point  $\tilde{\mathbf{p}}_{i,t}$ :

$$\begin{aligned} \tilde{\mathbf{p}}_{i,t} = & \tilde{\epsilon}_{i,t} \mathbf{p}_{i,t-1} + (1 - \tilde{\epsilon}_{i,t}) \mathbf{p}_{i,t+1} \\ & + g(\mathbf{p}_{i,t-1}, \mathbf{p}_{i,t+1}, \tilde{\epsilon}_{i,t}, \tilde{\varphi}_{i,t}) (\cos(\tilde{\psi}_{i,t}) \mathbf{r}_{i,t} \\ & + \sin(\tilde{\psi}_{i,t}) \mathbf{t}_{i,t} \wedge \mathbf{r}_{i,t}). \end{aligned}$$

where  $g = \|\mathbf{p}_{i,t} - \mathbf{p}_{i,t}^{\perp}\|$  is defined in Appendix A.

## 6. External forces computation

There exist in the literature many different expressions for computing external forces in a deformable model. A common approach is to combine a local and a global boundary term based on the gradient information (Delingette, 1999; Cohen et al., 1992) to estimate the location of structures of interest. In some cases, boundary-based external forces may not be sufficient in which case one may use the grey-level or textural description of the inner and/or outer region (Debreuve et al., 2001; Cocquerez and Philipp, 1995; Ronfard, 1994) to improve the boundary detection.

In our case, we chose to compute the external force at a vertex as a vector directed along the vertex normal and

proportional to the distance between the current vertex position and the position of a boundary voxel. This boundary voxel is searched along the vertex normal direction and within a limited distance  $r$  from the current vertex position. The range value  $r$  may be computed as a fraction of the size of the structure to segment or as a fraction of the image size. A line-scanning algorithm, based on an extension of the Bresenham (1965) drawing line algorithm in 3D, determines the set of voxels that are visited along the normal direction. This algorithm is applied with classical type of images where voxels are cubic but also with images of cylindrical geometry (where voxels are hexahedra) which occur when handling tridimensional ultrasound images as in (Montagnat et al., 2003).

The computation of boundary voxels depends on the nature of the external force. We detail below two strategies for finding those boundary voxels:

- *Gradient-based force.*

Those forces are well suited for the segmentation of structures that appear with a high to medium contrast in SPECT, CT, or MR images. The gradient information (vector and norm) is computed from the source image with standard differential operators. Based on the previously described line scanning algorithm in the gradient image, a voxel is considered to be a boundary voxel if it corresponds to a high gradient value (above a given threshold determined from the gradient histogram). If the structure of interest appears to be brighter or darker than surrounding structures, then the sign of the dot product between the gradient vector at a voxel and the normal direction at a vertex can be taken into account to discard spurious boundary voxels. More details are provided in (Delingette, 1999).

- *Region-based force.*

When dealing with low contrasted structures or when handling US images subject to high speckle, the gradient-based criterion is not appropriate to find relevant boundary points. In such cases, we combine region and boundary information to improve the boundary detection. In this formulation, a region is defined as a sequence of consecutive voxels whose intensity belongs to a user-defined intensity range. We further restrict the definition by imposing that a region must have a minimum number of voxels. The boundary voxel are then found to be the voxels that are the extremities of this region and whose gradient norm is greater than a threshold. In practice, it is sufficient to define a single region corresponding either to the structure to segment or to the neighboring structure. Furthermore, when the image is strongly anisotropic, we perform a trilinear interpolation of intensities for a better approximation of the true intensity profiles. Also, in case of highly texture images, it is possible to perform an anisotropic filtering (Weickert, 1998) of the intensity

profile leading to a smoothing of the profile except at parts of high gradient.

## 7. Application to cardiac images segmentation

The assessment of the cardiac function is important for the understanding and the early diagnosis of heart pathologies. In this section, we illustrate the concept of 4D deformable models with the segmentation of the myocardium and the LV chamber from 4D cardiac imagery. Based on volume estimation of the LV chamber along the cardiac cycle, the *Ejection Fraction* (EF) can be computed. The EF is an important clinical parameter measuring the ratio of blood ejected between the *End of Diastole* (ED: end of filling phase of the myocardium) and the *End of Systole* (ES: end of ejection phase). The ejection fraction value is typically  $70 \pm 10\%$  on healthy patients but is known to decrease significantly in the presence of some cardiac pathologies (Davis et al., 1993). Other quantitative parameters of cardiac dynamic could be extracted such as the septum wall thickness or the displacement of myocardium points.

### 7.1. Model measurements accuracy

The validation of segmentation outcome is a complex issue in medical imaging due to the lack of ground truth measurements for most applications (Bae et al., 1993; Bello and Colchester, 1998). To assess the accuracy of our segmentation algorithm, we propose to segment synthetic SPECT images generated by the NCAT simulator of Segars et al. (1999). NCAT images are produced by simulation of SPECT physics on a realistic spline-based dynamic heart phantom. The simulator produces gray level images and outputs multiple information about the observed objects, including the volume of each structure. The NCAT simulator produces realistic images in terms of geometry and physiology, although they tend to be more sharp and less noisy than real images.

For our case study, the left ventricle appear with a high intensity, while surrounding structures appear with

a lower contrast. 10 image sequences have been generated simulating different heart shapes by changing the heart scale and the ratio parameters. Images of the torso generated by the simulator are cropped around the LV area, resulting in volumes of  $42 \times 46 \times 30$  isotropic voxels ( $0.3125^3 \text{ cm}^3$ ). Each sequence is composed of 8 frames covering one heart cycle. Fig. 4 shows 4 images (middle slice at the end of diastole) randomly selected out of the 10 simulated sequences. On the same figure are shown the associated meshes representing the LV myocardium (at the end of diastole) and the LV chamber (at the end of systole) extracted from these 4 images with our segmentation algorithm.

The segmentation algorithm is based on the deformation of 4D simplex meshes in a coarse to fine manner as previously described. We use two additional set of 4D images to test what is the best sequence of deformation stages (from global to local) and what are the best values of locality parameter ( $\lambda$ ), the external force weight ( $\beta$ ), the surface rigidity ( $s$ ), and the force computation range ( $r$ ) for each stage. Once this manual tuning is done, we use the same sequence with the same parameter values for the segmentation of the 10 simulated 4D images. Table 2 shows the value of the algorithm parameters during each deformation stage. The deformation of the 4D simplex mesh is first highly constrained (rigid, similarity and finally affine registration is performed) with strong influence of external forces. A deformation sequence terminates when the 4D mesh does not move significantly between two iterations. After the affine registration, the mesh is close enough to the myocardium boundaries to start a globally constrained deformation with a lower influence of external forces.

Fig. 5 displays quantitative results. On the left, the diagram shows the LV myocardium volume (dashed lines) and the LV chamber volume (solid line) in the second image sequence. In each case, the thick line corresponds to the ground truth (the volume given by the simulator) and the thin line corresponds to the estimated volume of the deformed 4D model. It can be seen that, as expected, the myocardium volume has a very small variation during the heart cycle, while the LV chamber contracts significantly. From the LV chamber volume curve, the EF can be computed. On the right of Fig. 5

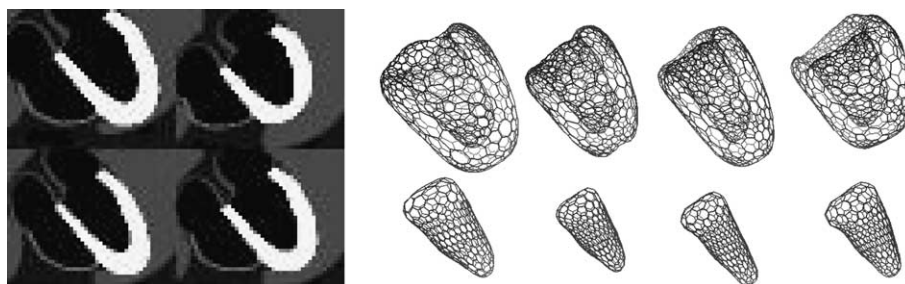


Fig. 4. Left: Four simulated SPECT images; Right: simplex meshes of the LV myocardium at ED (top) and the LV chamber ES (bottom).

Table 2  
The parameters associated with the five distinct stages of the segmentation algorithm

Deformation stage	Constraint	$\lambda$	$\beta$	$r$	$s$	# of iterations
Global deformation	Rigid	0	1	8		25
Global deformation	Similarity	0	1	6		15
Global deformation	Affine	0	1	3		90
Strongly constrained	Affine	0.2	0.1	2	5	30
Weakly constrained	Affine	0.5	0.1	2	3	20

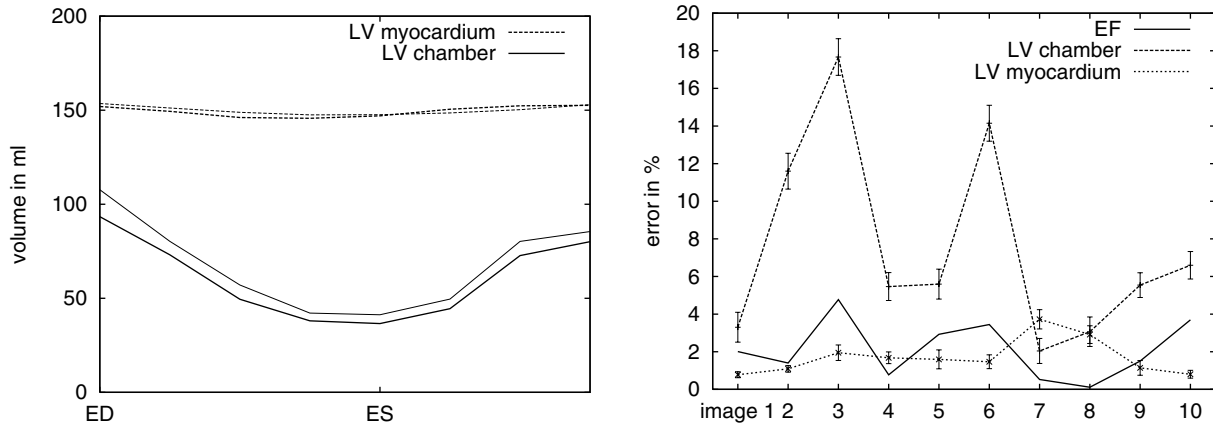


Fig. 5. Left: Volume of LV myocardium and chamber on sequence 2. Right: Mean error (in % of volume) in measuring the LV myocardium volume, the LV chamber volume, and the EF.

are displayed the average errors (expressed in % of the true volume) of the reconstructed volumes compared to the ground truth for the 10 simulated images. The volumes are averaged over the 8 instants and the error bars represent standard deviation around the means. The plain line shows the error (in %) of the computed ejection fraction compared to the ground truth.

This experience shows that the myocardium segmentation is fairly accurate on such good quality images. Over the 10 simulated images, the maximum error is below 4%. The LV chamber segmentation shows a more significant variation from the ground truth. This is because the definition of the LV chamber is geometrically ill-posed. Indeed we lack boundary information at the base of the left chamber boundary in SPECT images. In this case, it is the model shape constraints that prevent the leakage of the mesh in the region of the chamber base. Another alternative for estimating the LV chamber could have been to compute the volume enclosed by the LV myocardium after “closing” the ventricle at the base level.

Anyway, errors are quite consistent over a given sequence (the error variance is quite low although the absolute error can reach 17% in the worst case). It results in an accurate measurement of the EF (4.7% in the worst case, which is low compared to pathological variations of the EF).

In addition to volume measurements, Fig. 6 shows the local distance between the recovered myocardium surfaces and the reference surfaces extracted by isosurface computation from the original NCAT images. The distances are computed using the M.E.S.H. software (*Measuring Error between Surfaces using the Hausdorff distance*) developed at EPFL by [Aspert et al. \(2002\)](#). This tool measures the asymmetric distance between two discrete surfaces (triangular meshes) using the Hausdorff distance. It provides the maximum, mean and root-mean-square (RMS) errors between two given surfaces. Left of Fig. 6 displays an example of surface comparison for the 3rd frame of image 7 in our experiments (the worst case). The colors displayed on the myocardium surface are related to the distance between the surface recovered by the segmentation algorithm and the reference surface as computed by MESH. Darker values correspond to highest distances (up to 3.5 voxels in this case) and brighter values correspond to lowest distances. The maximum error are concentrated at the border of the base and at the apex where the mesh curvature is maximum and the smoothing constraint tends to bias the shape recovery. The diagram on the right of Fig. 6 shows the average distance (plain line with error bars corresponding to minimum and maximum distances) and the RMS distance (dashed line) between the recovered models and the reference surfaces

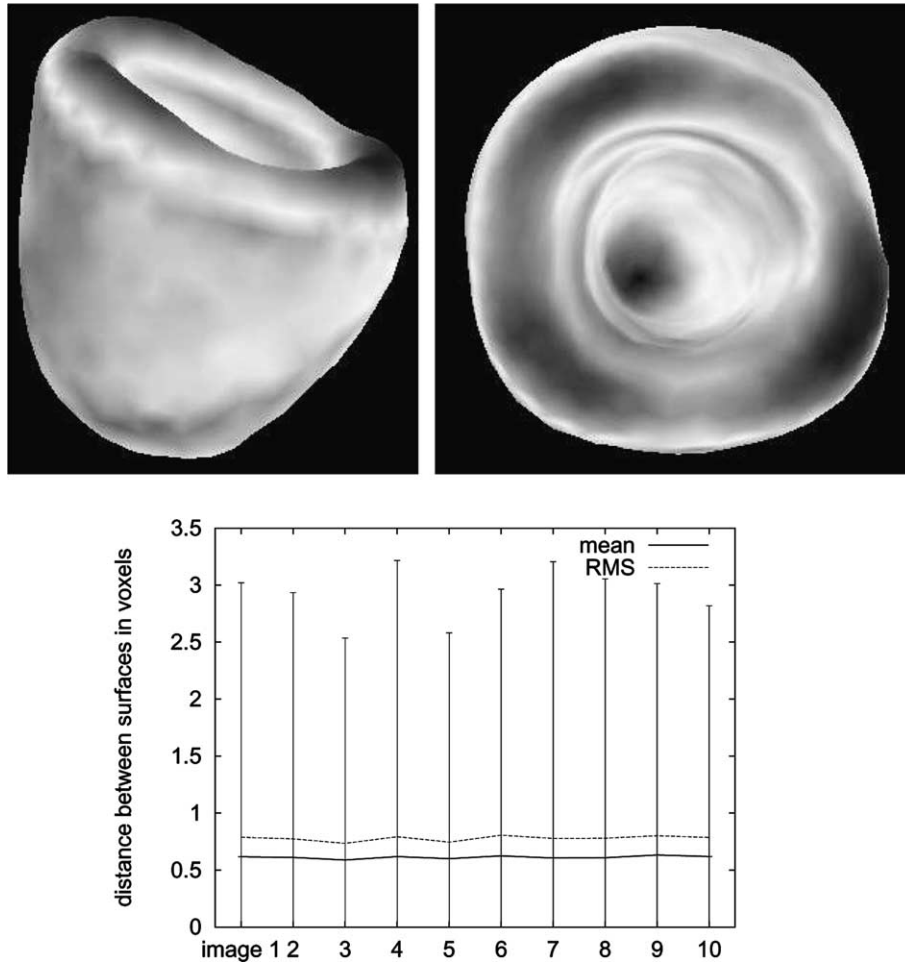


Fig. 6. Top: color distance map. Bottom: mean and RMS distance between the recovered surface and an isosurface extracted from the NCAT source images.

provided to the NCAT simulator for each of the 10 sequences studied. For each sequence, the 4 values displayed (minimum, maximum, mean and RMS distance) have been averaged over the 8 time frames. This figure shows that the average distance is always lower than a voxel with local maxima around 3 voxels. The recovered surfaces are therefore mostly located close to the reference surfaces up to a subvoxel distance. Thus, the model accuracy is demonstrated both in local (inter-surface distances) and global (volume) measures.

### 7.2. Non-synthetic image segmentation

We have segmented SPECT images having a resolution of  $64^3$  voxels ( $2 \times 2 \times 2$  mm voxels). SPECT sequences are covering one heart cycle over 8 time frames similarly to simulated images. The 4D cup-shaped LV myocardium model built for simulated images and shown on top of Fig. 8 is also used for segmenting those images. It consists of 500 vertices which is

well suited to the representation of the LV in low resolution SPECT images.

We have processed a SPECT image database provided by Professor Goris from Stanford Medical School. We compared images of 5 healthy patients with normal endocardium blood perfusion and one pathological patient with an abnormal perfusion due to ischemic zones.

Due to the high contrast of the LV in SPECT images, gradient forces are chosen as external forces. The 4D model is roughly initialized in a given reference position. Rigid followed by similarity registration are first performed to compensate for the differences in location and size between patients. Globally constrained deformations based on affine transformation are then applied. By progressively increasing the locality factor and lowering the external forces range, local deformations only affect a restricted neighborhood. Table 3 shows the different stages and the set of parameters used for each stage.

Table 3

Deformation stage	$\lambda$	Constraint	$\beta$	$\delta$	$s$	$r$	# of iterations
Global deformation	0	Rigid	1			5	35
Global deformation	0	Similarity	1			5	15
Strongly constrained	0.2	Affine	0.1	0.2	5	4	20
Weakly constrained	0.5	Affine	0.1	0.2	3	2	20
Local deformation	0.7	Affine	0.1	0.1	2	2	20

The segmentation of a pathological case is performed in the same way than healthy cases. Due to the poor perfusion of the myocardium in some pathologies the image contrast is much lower and the contours are weaker. The model rigidity then becomes critical for a

proper reconstruction of the heart boundaries. Fig. 7 shows the intersection of the deformed 4D model with 4 short axis slices of the pathological patient SPECT image. This figures compare the segmentation outcome with (left figure) and without (right figure) temporal constraints. Clearly segmentation errors are larger without temporal constraints (see the endocardium in slice 26 at time 2, or the epicardium at slice 32 time 4 for instance).

Fig. 8 shows a frontal view of the 4D models. The figure shows the reference model (top), a healthy patient model (center) and the pathological patient model (bottom). The deformed models in 4D show a much more regular aspect than the reference model obtained by 3D segmentation. The periodic nature of the motion

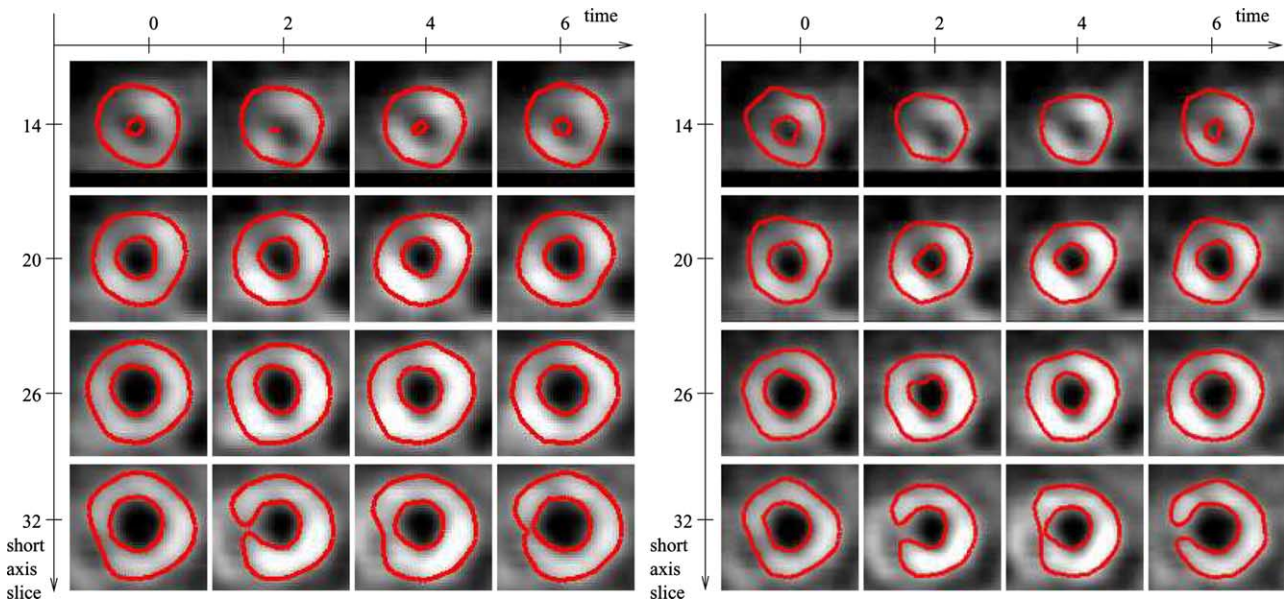


Fig. 7. 4D model deformed with (left) and without (right) time constraints.

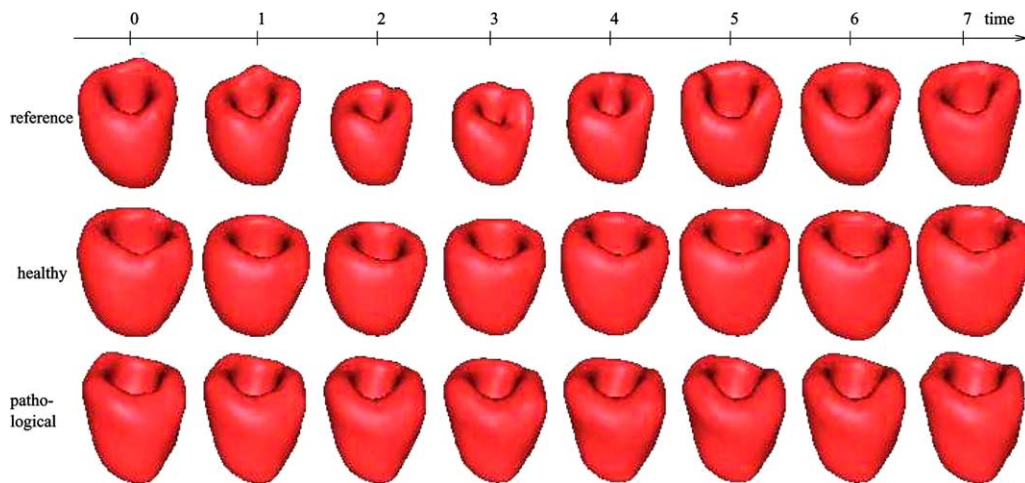


Fig. 8. Myocardium 4D models. From top to bottom: reference model obtained by 3D segmentation (top), healthy case (center), and pathological case (bottom).

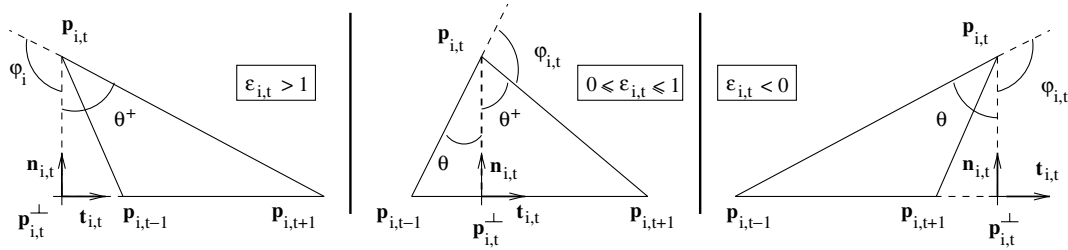


Fig. 9. Three possible cases for determining the position of a point relatively to its neighbors.

clearly appears between the first and the last instant for the 4D deformed models (center and bottom line). Also the difference in the motion amplitude between healthy and pathological cases clearly appears on the reconstructed surfaces.

### 7.3. Other modalities

The model presented so far is not modality-specific and can be used for different 3D image sequences segmentation. We have experimented this 4D deformable model for the segmentation of Magnetic Resonance (MR) and Ultrasound (US) images. Cardiac MR images have a very high in-slice resolution. However, the third dimension resolution is much lower ( $256 \times 256 \times 9$  for a voxel size of the order of  $0.5 \times 0.5 \times 8$  mm). 4D echocardiographic images are acquired with a rotative probe leading to a low spatial resolution ( $256 \times 256 \times 9$ , with a  $20^\circ$  angle between consecutive slices) and a high in-slice resolution ( $0.5 \times 0.5$  mm). The US image sequences are composed of 8 time points covering only the systole while the MR (13 time points) sequences cover the complete heart cycle. In these image sequences, the internal wall of the LV is reconstructed by a closed surface representing the internal blood volume.

The deformation process had to be adapted to each image modality. MR images offer a high contrast and two deformation stages (one affine registration followed by a local affinely constrained deformation) were sufficient to correctly segment the sequences starting from a 4D ellipsoid roughly centered on the LV. External forces are computed using the image gradient. The speckle appearing in ultrasound images and the lack of beam reflection on boundaries tangent to the ultrasound rays make the segmentation process more difficult. In a first registration stage, the gradient information is sufficient to steer the model since it is strongly constrained. After registration, the model locally deforms with an affine global constraint. Local deformations guided by region based forces with a restricted range and a weak surface rigidity are taking place in the final stage of the segmentation. Due to the approximate shape of the model a temporal smoothing constraint is used. Although preliminary results are promising, we were

not able to quantify the influence of temporal constraints due to the lack of ground truth segmentation.

## 8. Conclusion

In this paper, we have extended the deformable model framework to tackle the segmentation of 4D images by introducing temporal regularizing constraints in addition to spatial regularizing constraints. Weak or strong priors can be introduced about the motion of the model. With weak prior the vertex trajectories are smoothed by temporal averaging whereas with strong prior, the vertex trajectories are constrained to stay close to given reference trajectories. Those temporal forces tend to improve the segmentation of 4D medical images by improving its robustness against noise and outliers.

The segmentation accuracy was evaluated on simulated SPECT images for which a ground truth (organ surfaces and volumes) is known. We have shown a sub-voxel accuracy in the segmentation of the LV surface and LV chamber volume which is sufficient for clinical assessment of the cardiac function. Application of the 4D segmentation algorithm to non-synthetic SPECT, MR and US images have shown the versatility of our approach.

To increase the accuracy of the segmentation for a given image modality, it is possible to specify different set of parameters (rigidity, locality) at different parts of the mesh, for instance near the base of the LV or the apex of the endocardium where high curvature points makes the surface deformation more difficult to control. For image modalities like MR or US, more sophisticated external force definition based on the matching of intensity profiles (Cootes et al., 1995) or blocks (Sermesant et al., 2003) can also significantly improve the detection of image boundaries.

Moreover, the segmentation robustness can also be strengthened, especially when dealing with patient with strong pathologies, by relying on statistical shape appearance modeling for firing alarms when the current shape and image model is far from the expected one (Pitiot et al., 2003). In such case, one can decide to start again the segmentation based on a different initial model or with different set of parameters.

## Acknowledgements

We thank Professor M. Goris at Stanford Medical School for providing the SPECT images used in this paper.

## Appendix A

This appendix details the computation of temporal forces with prior motion knowledge as defined in section 5.2. The position  $\mathbf{p}_{i,t}$  of a vertex is related to the position of its temporal neighbors and the three parameters  $\varepsilon_{i,t}$ ,  $\varphi_{i,t}$ , and  $\psi_{i,t}$  by

$$\begin{aligned} \mathbf{p}_{i,t} &= \varepsilon_{i,t}\mathbf{p}_{i,t-1} + (1 - \varepsilon_{i,t})\mathbf{p}_{i,t+1} \\ &\quad + g(\mathbf{p}_{i,t-1}, \mathbf{p}_{i,t+1}, \varepsilon_{i,t}, \varphi_{i,t})(\cos(\psi_{i,t})\mathbf{r}_{i,t} \\ &\quad + \sin(\psi_{i,t})\mathbf{t}_{i,t} \wedge \mathbf{r}_{i,t}), \end{aligned}$$

where  $g = \|\mathbf{p}_{i,t} - \mathbf{p}_{i,t}^\perp\|$  is the height of  $\mathbf{p}_{i,t}$  above segment  $[\mathbf{p}_{i,t-1}, \mathbf{p}_{i,t+1}]$  (refer to Fig. 3 for an illustration of the geometric parameters composing a trajectory).

The height  $g$  is estimated differently in the three cases shown in Fig. 9 representing a local projection of the trajectory in plane  $(\mathbf{p}_{i,t-1}, \mathbf{p}_{i,t}, \mathbf{p}_{i,t+1})$ . In each case, the elevation angle is defined differently.

Let us define the following angles:  $\theta^+ = \angle \mathbf{p}_{i,t}^\perp \mathbf{p}_{i,t} \mathbf{p}_{i,t+1}$  and  $\theta^- = \angle \mathbf{p}_{i,t-1} \mathbf{p}_{i,t} \mathbf{p}_{i,t}^\perp$ .

- *First case:*  $\varepsilon_{i,t} > 1$

The elevation angle equals to  $\varphi_{i,t} = \pi - \theta^+$ , thus

$$\begin{aligned} \tan(\varphi_{i,t}) &= -\tan(\theta^+) \\ &= -\frac{\|\mathbf{p}_{i,t}^\perp - \mathbf{p}_{i,t+1}\|}{g} = -\frac{|\varepsilon_{i,t}|\|\mathbf{p}_{i,t+1} - \mathbf{p}_{i,t-1}\|}{g} \end{aligned}$$

leading to

$$g(\varepsilon_{i,t}, \varphi_{i,t}, \mathbf{p}_{i,t+1}, \mathbf{p}_{i,t-1}) = \frac{-\varepsilon_{i,t}\|\mathbf{p}_{i,t+1} - \mathbf{p}_{i,t-1}\|}{\tan(\varphi_{i,t})}.$$

- *Second case:*  $0 \leq \varepsilon_{i,t} \leq 1$

In that case, the equality  $\varphi_{i,t} = \pi - \theta^+ - \theta^-$  leads to

$$\begin{aligned} -\tan(\varphi_{i,t}) &= \tan(\theta^+ + \theta^-) = \frac{\tan(\theta^+) + \tan(\theta^-)}{1 - \tan(\theta^+)\tan(\theta^-)} \\ &= \frac{\|\mathbf{p}_{i,t+1} - \mathbf{p}_{i,t-1}\|g}{g^2 + \|\mathbf{p}_{i,t}^\perp - \mathbf{p}_{i,t-1}\|\|\mathbf{p}_{i,t}^\perp - \mathbf{p}_{i,t+1}\|}. \end{aligned}$$

This equation admits two values for  $g$ :

$$g = \frac{\|\mathbf{p}_{i,t+1} - \mathbf{p}_{i,t-1}\|}{2 \tan(\varphi_{i,t})} \left( -1 \pm \sqrt{1 + 4\varepsilon_{i,t}(1 - \varepsilon_{i,t})\tan^2(\varphi_{i,t})} \right).$$

One of those two solutions is always negative and the other one, the only acceptable, is always positive. If  $\varphi_{i,t} < \frac{\pi}{2}$ , the first term of  $g$  is positive and the second

one has to be positive as well. Else, the second term has to be negative:

$$\begin{aligned} g(\varepsilon_{i,t}, \varphi_{i,t}, \mathbf{p}_{i,t+1}, \mathbf{p}_{i,t-1}) \\ = \frac{\|\mathbf{p}_{i,t+1} - \mathbf{p}_{i,t-1}\|}{2 \tan(\varphi_{i,t})} \left( -1 + \varepsilon \sqrt{1 + 4\varepsilon_{i,t}^2 \tan^2(\varphi_{i,t})} \right) \end{aligned}$$

where

$$\varepsilon = \begin{cases} +1 & \text{if } \varphi_{i,t} < \frac{\pi}{2}, \\ -1 & \text{else} \end{cases}$$

- *Third case:*  $\varepsilon_{i,t} < 0$

The elevation angle is such that  $\varphi_{i,t} = \pi - \theta^-$ , thus

$$\begin{aligned} \tan(\varphi_{i,t}) &= -\tan(\theta^-) = -\frac{\|\mathbf{p}_{i,t}^\perp - \mathbf{p}_{i,t-1}\|}{g} \\ &= -\frac{|1 - \varepsilon_{i,t}|\|\mathbf{p}_{i,t+1} - \mathbf{p}_{i,t-1}\|}{g} \end{aligned}$$

leading to

$$g(\varepsilon_{i,t}, \varphi_{i,t}, \mathbf{p}_{i,t+1}, \mathbf{p}_{i,t-1}) = \frac{(\varepsilon_{i,t} - 1)\|\mathbf{p}_{i,t+1} - \mathbf{p}_{i,t-1}\|}{\tan(\varphi_{i,t})}.$$

## References

- Aspert, N., Santa-Cruz, D., Ebrahimi, T., Aug. 2002. MESH: Measuring error between surfaces using the Hausdorff distance. In: Proceedings of the IEEE International Conference on Multimedia and Expo (ICME'02), vol. I. Lausanne. <http://mesh.epfl.ch/>.
- Bae, K., Giger, M., Chen, C.-T., Khan, C., 1993. Automatic segmentation of liver structure in CT images. Medical Physics 20 (1), 71–78.
- Bardinet, E., Cohen, L., Ayache, N., 1996. Tracking and motion analysis of the left ventricle with deformable superquadrics. Medical Image Analysis 1 (2), 129–149.
- Bello, F., Colchester, A., 1998. Measuring global and local spatial correspondence using information theory. Medical Image Computing and Computer-Assisted Intervention (MICCAI'98). Lecture Notes in Computer Science, vol. 1496. Springer, Cambridge, USA.
- Benayoun, S., Ayache, N., 1998. Dense non-rigid motion estimation in sequences of medical images using differential constraints. International Journal of Computer Vision 26 (1), 25–40.
- Besl, P., McKay, N., 1992. A method for registration of 3D shapes. IEEE Transactions on Pattern Analysis and Machine Intelligence 14 (2), 239–256.
- Blake, A., Zisserman, A., 1987. Visual Reconstruction. MIT Press, New York.
- Bresenham, J., 1965. Algorithm for computer control of a digital plotter. IBM System Journal 4 (1), 25–30.
- Chandrashekhara, R., Rao, A., Sanchez-Ortiz, G.I., Mohiaddin, R.H., Rueckert, D., Jul. 2003. Construction of a statistical model for cardiac motion analysis using non-rigid image registration. In: Proceedings of the 18th International Conference On Information Processing in Medical Imaging (IPMI'03).
- Charnoz, A., Lingrand, D., Montagnat, J., 2003. A levelset based method for segmenting the heart in 3D+T gated SPECT images. International Workshop on Functional Imaging and Modeling of the Heart (FIMH'03). Lecture Notes in Computer Science, vol. 2674. Springer, Lyon, France.
- Cocquerez, J.-P., Philipp, S., 1995. Analyse d'images: filtrage et segmentation. Masson.

- Cohen, I., Cohen, L., Ayache, N., 1992. Using deformable surfaces to segment 3-d images and infer differential structures. *Computer Vision, Graphics, and Image Processing: Image Understanding* 56 (2), 242–263.
- Cootes, T., Taylor, C., Cooper, D., Graham, J., 1995. Active shape models, their training and application. *Computer Vision and Image Understanding* 61 (1), 38–59.
- Davis, M., Rezaie, B., Weiland, F., 1993. Assessment of left ventricular ejection fraction from technetium-99m-methoxy isobutyl isonitrile multiple gated radionuclide angiocardiology. *IEEE Transactions on Medical Imaging* 12 (2), 189–199.
- Debreuve, E., Barlaud, M., Aubert, G., Laurette, I., D., J., 2001. Space-time segmentation using level set active contours applied to myocardial gated SPECT. *IEEE Transactions on Medical Imaging* 20 (7), 643–659.
- Declercq, J., Feldmar, J., Ayache, N., 1998. Definition of a 4D continuous planispheric transformation for the tracking and the analysis of LV motion. *Medical Image Analysis* 2 (2), 197–213.
- Delingette, H., Jul. 1994. Modélisation, déformation et reconnaissance d'objets tridimensionnels à l'aide de maillages simplexes. Ph.D. thesis, École Centrale de Paris, France.
- Delingette, H., 1999. General object reconstruction based on simplex meshes. *International Journal of Computer Vision* 32 (2), 111–146.
- Frangi, A., Niessen, W., Viergever, M., 2001. Three-dimensional modeling for functional analysis of cardiac images: A review. *IEEE Transactions on Medical Imaging* 20 (1), 2–25.
- Frangi, A.F., Rueckert, D., Schnabel, J.A., Niessen, W.J., 2002. Automatic construction of multiple object three-dimensional statistical shape models: Application to cardiac modeling. *IEEE Transactions on Medical Imaging* 21 (9), 1151–1166.
- Gérard, O., Collet-Billon, A., Rouet, J.-M., Jacob, M., Fradkin, M., Allouche, C., 2002. Efficient model-based quantification of left ventricle function in 3D echocardiography. *IEEE Transaction in Medical Imaging* 21 (9), 1059–1068.
- Lin, N., Yu, W., Duncan, J.S., 2002. Combinative multi-scale level set framework for echocardiographic image segmentation. In: Dohi, T., Kikinis, R. (Eds.), *Proceedings of MICCAI 2002: Fifth International Conference on Medical Image Computing and Computer-Assisted Intervention*. Lecture Notes in Computer Science, vol. 2488. Springer, Tokyo.
- Löjtjönen, J., Reissman, P.-J., Magnin, I., Katila, T., 1999. Model extraction from magnetic resonance volume data using the deformable pyramid. *Medical Image Analysis* 3 (4), 387–406.
- McInerney, T., Terzopoulos, D., 1995. A dynamic finite element surface model for segmentation and tracking in multidimensional medical images with application to cardiac 4D image analysis. *Computerized Medical Imaging and Graphics* 19 (1), 69–83.
- McInerney, T., Terzopoulos, D., 1996. Deformable models in medical image analysis: a survey. *Medical Image Analysis* 1 (2), 91–108.
- Montagnat, J., Delingette, H., 1998. Globally constrained deformable models for 3D object reconstruction. *Signal Processing* 71 (2), 173–186.
- Montagnat, J., Delingette, H., Malandain, G., 1999. Cylindrical echocardiographic images segmentation based on 3D deformable models. *Medical Image Computing and Computer-Assisted Intervention (MICCAI'99)*. Lecture Notes in Computer Science, vol. 1679. Springer, Cambridge, UK.
- Montagnat, J., Delingette, H., Ayache, N., 2001. A review of deformable surfaces: topology, geometry and deformation. *Image and Vision Computing* 19 (14), 1023–1040.
- Montagnat, J., Sermesant, M., Delingette, H., Malandain, G., Ayache, N., 2003. 4D Cylindrical echocardiographic images anisotropic filtering for model based segmentation. *Pattern Recognition Letters* 24 (4–5), 815–828.
- Nastar, C., Ayache, N., 1996. Frequency-based nonrigid motion analysis: Application to four dimensional medical images. *IEEE Transactions on Pattern Analysis and Machine Intelligence* 18 (11), 1067–1079.
- Papademetris, X., Sinuas, A., Dione, D., Duncan, J., 2001. Estimation of 3D left ventricular deformation from echocardiography. *Medical Image Analysis* 5 (1), 17–28.
- Paragios, N., 2002. A variational approach for the segmentation of the left ventricle in cardiac image analysis. *International Journal of Computer Vision* 50 (3), 345–362.
- Park, J., Metaxas, D., Axel, L., 1996. Analysis of left ventricular motion based on volumetric deformable models and MRI-SPAMM. *Medical Image Analysis* 1 (1), 53–71.
- Pennec, X., 1996. L'incertitude dans les Problèmes de Reconnaissance et de Recalage. Application en Imagerie Médicale et Biologie Moléculaire. Ph.D. thesis, École Polytechnique, France.
- Pham, Q., Vincent, F., Clarysse, P., Croisille, P., Magnin, I., 2001. A FEM-based deformable model for the 3D segmentation and tracking of the heart in cardiac MRI. In: *International Symposium on Image and Signal Processing and Analysis*. Pula, Croatia.
- Pitiot, A., Delingette, H., Ayache, N., Thompson, P., 2003. Expert-knowledge-guided segmentation system for brain MRI. In: Ellis, R.E., Peters, T.M. (Eds.), *Medical Image Computing and Computer-Assisted Intervention MICCAI'03*. Vol. 2879 of LNCS. Springer Verlag, Montreal.
- Ronfard, R., 1994. Region-based strategies for active contour models. *International Journal of Computer Vision* 13 (2), 229–251.
- Segars, W., Lalush, D., Tsui, B., 1999. A realistic spline-based dynamic heart phantom. *IEEE Transactions on Nuclear Science* 46 (3), 503–506.
- Sermesant, M., Coudière, Y., Delingette, H., Ayache, N., 2002. Progress towards an electro-mechanical model of the heart for cardiac image analysis. In: *IEEE International Symposium on Biomedical Imaging (ISBI'02)*.
- Sermesant, M., Clatz, O., Li, Z., Lantéri, S., Delingette, H., Ayache, N., 2003. A parallel implementation of non-rigid registration using a volumetric biomechanical model. In: Gee, J., Maintz, J.A., Vannier, M.W. (Eds.), *Second International Workshop on Biomedical Image Registration WBIR'03*. Lecture Notes in Computer Science, vol. 2717. Springer, Philadelphia, PA.
- Terzopoulos, D., Metaxas, D., 1991. Dynamic 3D models with local and global deformations: deformable superquadrics. *IEEE Transactions on Pattern Analysis and Machine Intelligence* 13 (7), 703–714.
- Üzümcü, M., Frangi, A.F., Sonka, M., Reiber, J.H.C., Lelieveldt, B.P.F., Oct. 2003. Ica vs. pca active appearance models: Application to cardiac MR segmentation. In: *Medical Image Computing and Computer-Assisted Intervention (MICCAI'01)*.
- Vemuri, B., Radisavljevic, A., 1993. From Global to Local, a Continuum of Shape Models with Fractal. In: *International Conference on Computer Vision and Pattern Recognition (CVPR'93)*. New York, USA.
- Weickert, J., 1998. *Anisotropic Diffusion in Image Processing*. Teubner-Verlag.